

3-D Imaging and Inverse Labeling of Biological Samples Based on Reflectance-Guided Adaptive Fringe Projection

Ziqiang Wei¹, Sudong Ding¹, Yan Hu¹, Shuang Mu², Kehui Wang³, Kun Gui³,
Shijie Feng¹, *Member, IEEE*, Qian Chen¹, and Chao Zuo¹, *Senior Member, IEEE*

Abstract—Vision-based 3-D measurement techniques play a crucial role in capturing and restoring the realism of scenes. However, when measuring objects with significant reflectance variance, the captured image is prone to saturation, leading to errors and incomplete or malformed 3-D data. This article presents an effective and robust adaptive fringe projection method specifically designed for measuring high dynamic samples with highlighted surfaces. Our approach iteratively reduces the light intensity at regions of the projected patterns corresponding to the highlighted surface in several steps, ensuring the full-field unsaturated intensity in the captured images. Then, the reflectance map is used to optimize the phase-shifted patterns further to reconstruct 3-D data, which has smoother contours than methods employing multiple exposures with numerous fringe images. By mapping the drawn lines on the sample image into the projected patterns, inverse labeling is performed by projecting positioning lines to guide the cutting of pathological samples. We carried out experiments on accuracy validation and comparison with other methods, and the results demonstrate that our proposed method accurately reconstructs complete 3-D profiles of highlight surfaces on biological samples and can project precise labeling lines with adjustable thicknesses and shapes.

Index Terms—3-D reconstruction, adaptive projection, fringe projection profilometry (FPP), highlight surface, inverse labeling.

Received 30 August 2024; revised 1 November 2024; accepted 25 November 2024. Date of publication 18 February 2025; date of current version 5 March 2025. This work was supported in part by the National Key Research and Development Program of China under Grant 2022YFB2804603 and Grant 2024YFF0505600, in part by the Young Elite Scientists Sponsorship Program by China Association for Science and Technology (CAST) under Grant 2022QNR001, in part by China Postdoctoral Science Foundation under Grant 2022M721619, in part by the National Natural Science Foundation of China under Grant 62005121 and Grant U21B2033, and in part by the Fundamental Research Funds for the Central Universities under Grant 30924010814. The Associate Editor coordinating the review process was Dr. Gordon Shaw. (Ziqiang Wei and Sudong Ding contributed equally to this work.) (Corresponding authors: Yan Hu; Chao Zuo.)

Ziqiang Wei, Sudong Ding, Yan Hu, Shijie Feng, and Chao Zuo are with Jiangsu Key Laboratory of Spectral Imaging and Intelligent Sense and the Smart Computational Imaging Laboratory (SCILab), Nanjing University of Science and Technology, Nanjing, Jiangsu 210094, China (e-mail: zi-qiang.wei@njust.edu.cn; dingsudong@njust.edu.cn; hu_yan@njust.edu.cn; shijiefeng@njust.edu.cn; zuochao@njust.edu.cn).

Shuang Mu is with Shanghai Aerospace Control Technology Institute, Shanghai 201109, China (e-mail: moushuang@803sast.com).

Kehui Wang and Kun Gui are with Konfoong Biotech International Company Ltd., Ningbo, Zhejiang 315499, China (e-mail: Kehui.wang@kfbio.cn; kun.gui@kfbio.cn).

Qian Chen is with Jiangsu Key Laboratory of Spectral Imaging and Intelligent Sense, Nanjing University of Science and Technology, Nanjing, Jiangsu 210094, China (e-mail: chenqian@njust.edu.cn).

Digital Object Identifier 10.1109/TIM.2025.3542863

I. INTRODUCTION

THE 3-D measurement technology can be categorized into contact and noncontact types. Contact methods, exemplified by the coordinate measuring machine, involve a probe touching the object's surface to acquire 3-D information point by point. This approach boasts micrometer-level accuracy but necessitates a stable testing environment. Furthermore, contact changes the object's physical properties [1]. In scenarios demanding noncontact measurement, optical methods offer a viable solution [2]. These techniques derive 3-D information from optical signals, enabling flexible surface shape sensing [3], [4], [5]. Optical-based methods encompass various approaches, including multi-(binocular)stereo vision [6], [7], time of flight [8], fringe projection profilometry (FPP) [9], [10], and others [11], [12], [13]. Among them, FPP is a promising technique, thanks to its noncontact, high flexibility, and full-field features.

A basic FPP system comprises a projector and a camera. The computer controls the projection of predesigned fringe maps onto the objects. Simultaneously, the camera captures and transmits the deformed fringe images to the computer. The coded phase information is then extracted from the captured fringe images. The absolute 3-D coordinates of the object are calculated by combining the system parameters obtained from a prior calibration process [14], [15], [16].

Measuring objects with highly reflective surfaces and a wide dynamic range of intensities presents unique challenges. These challenges are typically addressed through specialized techniques or algorithms, categorized as device-based [17] or algorithm-based [18], [19], [20], [21]. One approach pioneered by Yau [22] involves selecting the brightest yet unsaturated pixel from the captured image for pixel-by-pixel phase retrieval. This is achieved by systematically adjusting the exposure time from high to low. Building upon this concept, Rao and Da [23] introduced a fully automated multiexposure FPP technique. This method assesses the camera's noise level to determine a modulation threshold, subsequently guiding the automatic calculation of the required exposure time. Wang et al. [24] further investigated the influence of the surrounding light on the measured sample. They captured two additional sets of fringe patterns beforehand to estimate the appropriate exposure time interval. This enabled accurate 3-D reconstruction by selecting multiple exposure times and extracting

suitable pixels from the captured fringe sequence. Waddington and Kofman [25] proposed a method to dynamically adjust the maximum gray level based on ambient light and surface reflectance, effectively preventing image saturation. However, this approach takes time. Lin et al. [26] estimated each pixel's reflectance, ambient light intensity, and reflected light intensity, projected uniform gray maps at equal intervals, and calculated the optimal projected light intensity.

The Gray code method offers a means to achieve high-dynamic range 3-D measurement. It involves subpixel accurate fringe edge detection and projection intensity correction [27], [28]. Liu et al. [29] focused on measuring small, shiny objects by projecting high-intensity and low-intensity patterns. This allowed them to calculate the object's reflectance and generate appropriate projected intensities. Zhang et al. [30] estimated the projection intensity of the targets by projecting three uniform grayscale images. They established a mapping between the projected and captured images using a series of horizontal and vertical fringe patterns, ultimately achieving optimal fringe images.

Sun and Zhang [31] addressed the resolution differences between the camera and projector by creating a projection intensity model for each pixel. After establishing an accurate mapping relationship, adaptive fringe patterns were generated. Salahieh et al. [32] introduced a multipolarization technique by eliminating saturation and increasing the fringe contrast by selecting the proper polarized channel measurements. Zhao et al. [33] developed a digital micromirror device (DMD) modulation strategy based on the DMD camera to prevent saturation before acquiring phase-shifted images. Hu et al. [34] calculated the phase map of the highlighted region using a subset of phase-shifted fringe images. Their multifrequency phase-shifted scheme improved the integrity of the final phase map for highlighted surfaces. Zheng et al. [35] proposed using color cameras to respond to different channels of a single color fringe. Jiang et al. [36] devised a real-time system for high-contrast targets by projecting inverted patterns, enabling real-time and high-dynamic range 3-D imaging.

Existing adaptive projection techniques, while effective and practical, often necessitate complex operations and lengthy data calculations. This article introduces a new approach that simplifies the process by actively reducing the projection intensity corresponding to the overexposed regions using the reflectance information of the object surface. Our system first projects fringe patterns to obtain the absolute phase and then identifies overexposed areas by projecting the maximum input gray map. Next, we extract the boundary of the overexposed region, assuming the phase values along the outer edge of this boundary are correct. The 3-D location of the outer edge, as the boundary, is calculated and then mapped to the projector's DMD coordinate system. By connecting the discontinuous mapped pixels on DMD, we obtain connected regions, which can be single or multiple connected areas.

Within the newly defined region, the projector's global intensity is reduced by a certain level. This adjusted intensity generates a set of suitable fringe patterns for retrieving the 3-D measurement. Through several iterations, we automatically obtain unsaturated phase-shifted images and complete 3-D

data. Finally, a series of patterns with different gray values is projected to get the surface reflectance map, which is used to generate new patterns coupling better with the surface feature, thus improving the overall quality of the reconstructed 3-D data and producing a more realistic result. Based on this, we can map the pixels of lines drawn on the sample image to the DMD plane. By projecting these lines onto the samples, we achieve inverse labeling, which offers positioning guidance that enables remote experts to assist on-site operators in accurately cutting biological samples.

II. THEORY

This section introduces the theoretical foundation of our FPP system. We first explain the phase extraction process using the phase-shifting algorithm. Following this, we describe the calibration process, including accurately determining feature points. After calibrating device parameters and phase extraction, we describe how to leverage spatial constraints across different devices for 3-D reconstruction. Finally, we explain the mapping of marker pixels to the DMD plane, enabling the implementation of inverse labeling for biological samples.

A. Coordinate Systems of the Imaging Model

A typical FPP system comprises a projector and a camera. The fringe patterns are projected onto the samples while the camera simultaneously captures the images for subsequent processing. The camera adopts a pinhole imaging model as the following equation presents, corresponding to transforming world coordinates $P(X, Y, Z)$ to pixel coordinates $p(u, v)$:

$$s \begin{bmatrix} u \\ v \\ 1 \end{bmatrix} = \underbrace{\begin{bmatrix} f_x & 0 & u_0 \\ 0 & f_y & v_0 \\ 0 & 0 & 1 \end{bmatrix}}_A \underbrace{\begin{bmatrix} r_{11} & r_{12} & r_{13} & t_x \\ r_{21} & r_{22} & r_{23} & t_y \\ r_{31} & r_{32} & r_{33} & t_z \end{bmatrix}}_{R|T} \begin{bmatrix} X \\ Y \\ Z \\ 1 \end{bmatrix}. \quad (1)$$

Here, s denotes the perspective factor, A illustrates the camera's intrinsic parameters, R denotes the rotation vectors, T is a translation vector, and $P_{3 \times 4}$ stands for the whole projection matrix, integrating internal and external parameters.

B. Coded Phase Retrieval

The standard N -step phase-shifting algorithm extracts the phase values from a sequence of sinusoidal phase-shifting patterns. Here, c and p stand for camera and projector, respectively. The intensity values with a phase shift $2\pi/N$ for each pattern can be written as

$$I_n^p(u^p, v^p) = G(u^p, v^p) \times [a^p + b^p \cos(2\pi f^p u^p - \delta^n)]. \quad (2)$$

Here, $\delta^n = 2\pi n/N$, and the index $n(0, 1, \dots, N-1)$ signifies the order of the patterns used. $G(u^p, v^p)$ is the maximum input grayscale map. a^p and b^p represent the mean value and amplitude of the sinusoidal signals in the fringe, respectively. f^p is the fringe frequency. After the patterns are projected

onto the object, the intensity captured by the camera can be expressed as

$$I_n^c(u^c, v^c) = r(u^c, v^c) \{ I_n^p(u^p, v^p) + a \} + b. \quad (3)$$

Here, a represents the reflected intensity by ambient light, and b represents the ambient light intensity independent of the object. Depending on the object's position, r determines the reflectance and also the coordinates correspondence between (u^c, v^c) and (u^p, v^p) . Here, we rewrite (3) as

$$I_n^c(u^c, v^c) = A(u^c, v^c) + B(u^c, v^c) \cos[\phi(u^c, v^c) - \delta^n] \quad (4)$$

where $A(u^c, v^c)$ denotes the average intensity, $B(u^c, v^c)$ is the modulation, and $\phi(u^c, v^c)$ is the wrapped phase, which is to be calculated by

$$\phi(u^c, v^c) = \tan^{-1} \left[\frac{\sum_{n=1}^N I_n^c(u^c, v^c) \sin(\delta^n)}{\sum_{n=1}^N I_n^c(u^c, v^c) \cos(\delta^n)} \right]. \quad (5)$$

The obtained ϕ in this step has a truncated spatial distribution with 2π phase jumps. To address this issue, the multifrequency unwrapping algorithm is adopted [37], which utilizes the fringe patterns of different frequencies to obtain the unwrapped phase map $\Phi(u^c, v^c)$ through

$$\Phi(u^c, v^c) = \phi(u^c, v^c) + 2\pi k(u^c, v^c). \quad (6)$$

Here, $k(u^c, v^c)$ represents the fringe order, which can be derived from the phase relationship among multiple sets of fringe images with different frequencies.

C. System Calibration

The camera calibration process employs Zhang et al.'s [38] method. A four-step approach is implemented to ensure accurate projector calibration.

Step 1: Phase unwrapping. The projector projects fringe patterns in both horizontal and vertical directions with different frequencies and phase shifts onto the calibration board. These patterns are shown in Fig. 1(a), Φ_x and Φ_y (x and y denote the horizontal and vertical directions, respectively) are solved by (6).

Step 2: Feature point determination on the camera's coordinate system. The phase-shifting algorithm can extract a uniformly illuminated calibration pattern, which can also be obtained by illuminating an all-white pattern by the projector. Feature point extraction determines the coordinates of the corner points on the checkerboard grid in the camera's coordinate system, denoted by c_{ij} .

Step 3: Feature points determination on the projector's coordinate system. When determining the feature points, it is crucial to consider the phase error that occurs at the boundaries between black and white squares on the checkerboard. To solve this problem, we propose a feature point determination method that leverages the geometric center of the white squares.

The flow is illustrated in Fig. 1(b). First, c_{ij} are converted to the geometric center of the white squares on the checkerboard, noted by \bar{q}_{ij} . The conversion is accomplished by selecting the diagonal intersection of every four corner points of the squares. Inspired by the method in [39], within a $w \times w$ square

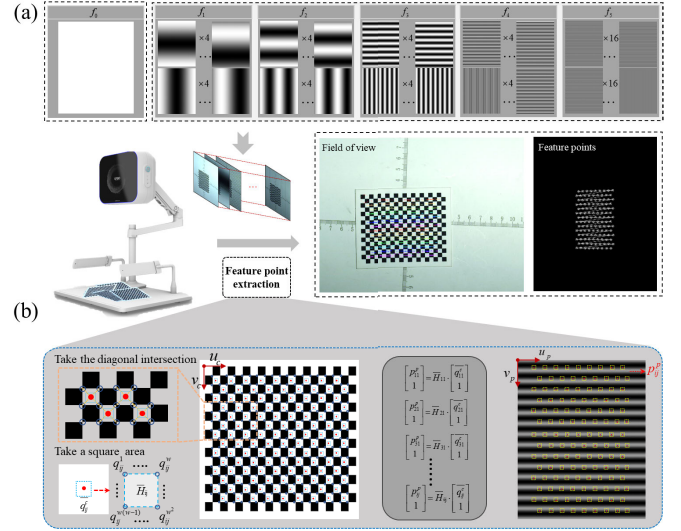


Fig. 1. Fringe patterns used and the method for determining feature points during calibration. (a) Phase maps are obtained from horizontal and vertical sinusoidal coded fringe patterns. (b) Feature point determination is based on the geometric center of the white squares on the checkerboard, utilizing homography transformations for projector calibration.

area centered on \bar{q}_{ij} , we select points starting from the upper left corner of the square area for $k = 1$ and progress to the lower right corner for $k = w^2$, denoted as $q_{ij}^k(u_c, v_c)$, and the corresponding point $p_{ij}^k(u_p, v_p)$ in the projector can be determined as

$$\begin{cases} u_p = \frac{\omega_x}{2\pi N_x} \cdot \Phi_x(u_c, v_c) \\ v_p = \frac{\omega_y}{2\pi N_y} \cdot \Phi_y(u_c, v_c). \end{cases} \quad (7)$$

Here, (Φ_x, Φ_y) at $q_{ij}^k(u_c, v_c)$ is obtained through the phase-shifting and unwrapping algorithms. (N_x, N_y) are the fringe numbers of the coded sinusoidal patterns and (ω_x, ω_y) is the pixel numbers of the DMD in two directions. Then, we can get the homography matrix \bar{H}_{ij} by minimizing the cost function as follows:

$$\bar{H}_{ij} = \arg \min_{H_{ij}} \sum_{\forall p_{ij}^k}^{k=1:w^2} \left\| \bar{q}_{ij} - H_{ij} \cdot p_{ij}^k \right\|^2 \quad (8)$$

where $\|\cdot\|$ is the least-squares distance. By applying the local homography matrix \bar{H}_{ij} , the feature point \bar{p}_{ij} on the projector is converted to the camera point \bar{q}_{ij} by

$$\bar{p}_{ij} = \bar{H}_{ij}^{-1} \cdot \bar{q}_{ij}. \quad (9)$$

This approach enhances the robustness of feature point coordinate extraction, ensuring that the phase error of a single point does not compromise the coordinates' accuracy.

Step 4: Calibration parameter acquisition. The calibration is performed by optimizing the parameters of feature points across different poses using the perspective-n-point method [40], which iteratively minimizes the difference between the observed points and the calculated points by

employing a cost function of

$$F_c = \min_{\text{avg}} \sum_{p_{ij}} \|p - \hat{p}(A, R, T, k)\|^2. \quad (10)$$

D. Pixel Mapping From the Camera to the Projector

After obtaining the calibration parameters, we can get the projection matrix for both the camera and projector as

$$P^c = A_c [R \ T] = \begin{bmatrix} p_{11}^c & p_{12}^c & p_{13}^c & p_{14}^c \\ p_{21}^c & p_{22}^c & p_{23}^c & p_{24}^c \\ p_{31}^c & p_{32}^c & p_{33}^c & p_{34}^c \end{bmatrix} \quad (11)$$

$$P^p = A_p [R \ T] = \begin{bmatrix} p_{11}^p & p_{12}^p & p_{13}^p & p_{14}^p \\ p_{21}^p & p_{22}^p & p_{23}^p & p_{24}^p \\ p_{31}^p & p_{32}^p & p_{33}^p & p_{34}^p \end{bmatrix}. \quad (12)$$

Given the camera coordinate $q(u^c, v^c)$, the projector's horizontal coordinate u^p can be obtained by (7); then, the 3-D point $P(X^W, Y^W, Z^W)$ can be calculated by

$$\begin{bmatrix} X^W \\ Y^W \\ Z^W \end{bmatrix} = \begin{bmatrix} p_{11}^c - p_{31}^c u^c & p_{12}^c - p_{32}^c u^c & p_{13}^c - p_{33}^c u^c \\ p_{21}^c - p_{31}^c v^c & p_{22}^c - p_{32}^c v^c & p_{23}^c - p_{33}^c v^c \\ p_{11}^p - p_{31}^p u^p & p_{12}^p - p_{32}^p u^p & p_{13}^p - p_{33}^p u^p \end{bmatrix}^{-1} \cdot \begin{bmatrix} p_{14}^c - p_{34}^c u^c \\ p_{24}^c - p_{34}^c v^c \\ p_{14}^p - p_{34}^p u^p \end{bmatrix}. \quad (13)$$

The mapped point $p(u^p, v^p)$ in the DMD plane can be derived by the following equation:

$$z^p \begin{bmatrix} u^p \\ v^p \\ 1 \end{bmatrix} = \begin{bmatrix} p_{11}^p & p_{12}^p & p_{13}^p & p_{14}^p \\ p_{21}^p & p_{22}^p & p_{23}^p & p_{24}^p \\ p_{31}^p & p_{32}^p & p_{33}^p & p_{34}^p \end{bmatrix} \begin{bmatrix} X^w \\ Y^w \\ Z^w \\ 1 \end{bmatrix}. \quad (14)$$

III. SYSTEM DESIGN AND METHODOLOGY

This section delves into an adaptive fringe projection algorithm designed to reconstruct sample surfaces exhibiting a high dynamic range of brightness based on a self-designed 3-D measurement system. Simply reducing the overall light intensity is impractical, as it compromises image quality, leading to a loss of detail and reduced contrast. Therefore, it becomes essential to adjust the projection intensity selectively in brighter areas without affecting the intensity in darker regions. To achieve this, we propose a step-by-step iterative approach for fine-tuning the brightness of the projected patterns to get the 3-D profile and a reflectance-guided adaptive fringe projection process to enhance local contrast while ensuring relatively uniform brightness across different regions. Based on the retrieved 3-D shape, remote guidance is achieved by inversely projecting interactive labeling onto the surface, enabling precise manipulation of local pathological samples.

A. System Architecture

The system setup is depicted in Fig. 2(a), in which we use an Imaging Source USB 3.0 camera DFK33UX183 with a resolution of 2560×1920 pixels equipped with an MVL-KF1624M-25MP zoom lens from Hikrobot and a

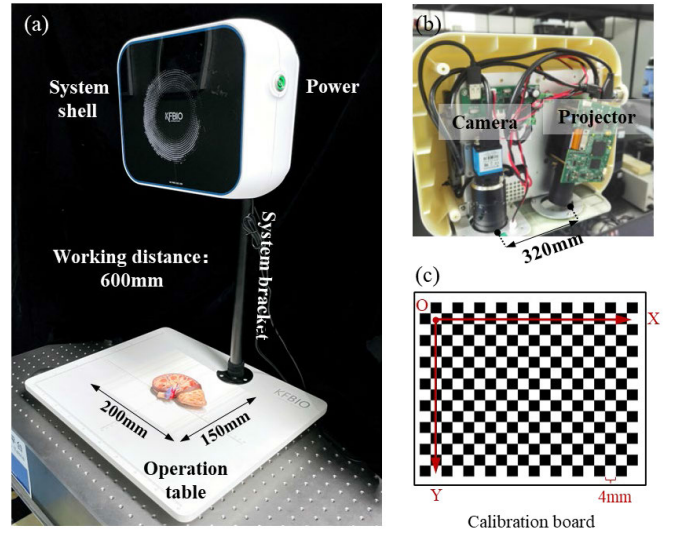


Fig. 2. Photographs of the experimental setup. (a) 3-D model design of the system. (b) Device and layout inside the shell. (c) Calibration board, featuring 20×16 units of 4 mm^2 .

TABLE I
INFORMATION OF THE USED PATTERNS WITH DIFFERENT FREQUENCIES

Items	Values			
i (order)	1	2	3	4
N_i (phase-shifting number)	4	4	8	1
f_i (Fringes frequency)	1	7	57	0

Pro4500CV digital projector with a maximum resolution of 1280×800 pixels, as shown in Fig. 2(b). The working system is housed within a specially designed shell with a working distance of 600 mm, enabling 3-D measurements within a field of view of 200×150 mm. The shell can be rotated around the system bracket, allowing for position adjustments for operator convenience.

Our system's calibration method is based on our previous work [9], and the calibration target utilized is provided in Fig. 2(c). The fringe parameters employed in our system are summarized in Table I. The first three columns represent sinusoidal phase-shifting patterns, while the fourth corresponds to a white uniform pattern used to obtain brightness distribution.

The system incorporates self-developed software that supports data acquisition and algorithm processing using CPU multithreading, GPU acceleration, and other parallel processing technologies. These optimizations are designed primarily to meet the speed requirements of real-world applications, ensuring the timely execution of algorithms. However, it is important to note that these acceleration techniques aim to improve processing speed and do not directly impact the accuracy of the imaging results.

B. Identification of Overexposed Regions

The projector first projects a maximum input grayscale G_{\max}^0 onto the sample, and the camera is synchronized to capture an image I^c , based on which we define a mask map R_c^i to identify

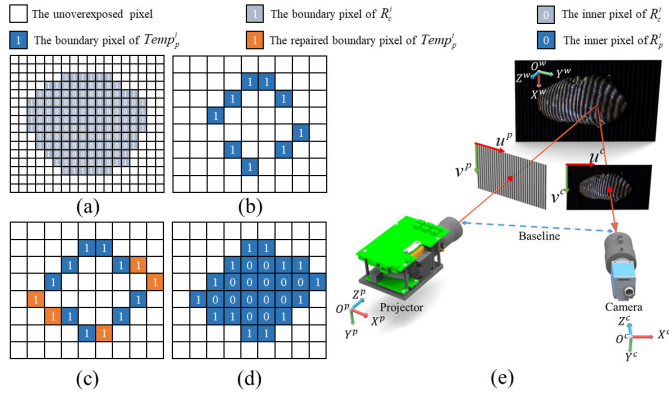


Fig. 3. Schematic illustrates the mapping process of the overexposed mask from the camera to the projector. (a) Overexposed mask in the image. (b) Boundary in the projector coordinates, mapped from the camera. (c) Boundary interpolation to obtain a closed region. (d) Overexposed mask in the DMD plane. (e) Correctly reconstructed boundary data are transformed between the imaging and projection coordinate systems.

the overexposed region as

$$R_c^i(u^c, v^c) = \begin{cases} 1, & I^c(u^c, v^c) \geq T \\ 0, & I^c(u^c, v^c) < T. \end{cases} \quad (15)$$

Here, T is the intensity threshold (e.g., 250 if 8-bit images were used). If $I^c(u^c, v^c)$ is greater than the threshold T , the mask value at $R_c^i(u^c, v^c)$ is set to 1 (here, i stands for the current iteration number). As summarized in Fig. 3, the boundaries of R_c^i are then extracted using the Canny operator and mapped to the DMD pixel coordinate, whose corresponding boundary pixels are noted as $Temp_p^i(u^p, v^p)$, which is then repaired to get a mask $R_p^i(u^p, v^p)$ with completely closed regions. The boundary mapping is based on transforming its correct 3-D data between the two coordinate systems, as shown in Fig. 3(e).

C. Adaptive Regeneration of Fringe Patterns

Reducing G_{\max} only once in the overexposed region is insufficient to eliminate saturation. Therefore, a gradual intensity reduction within the projection space is proposed to decrease the overexposed area dynamically. The process of determining regions with varying brightness is illustrated in Fig. 4, satisfying the following relation:

$$G_{\max}^i(u^p, v^p) = G_{\max}^{i-1}(u^p, v^p) - R_p^i(u^p, v^p) \times g. \quad (16)$$

Here, i is the iteration number and the grayscale reduction for the fringe patterns in each iteration. We set g to 60 in 8-bit patterns. Subsequently, new fringe patterns are regenerated by

$$I_n^p(u^p, v^p) = G_{\max}^i(u^p, v^p) \times [a^p + b^p \cos(2\pi f^p u^p - \delta^n)]. \quad (17)$$

Fig. 4 visually depicts the dynamic adjustment throughout the iterative process. When no valid points exist in $R_p^i(u^p, v^p)$, it indicates no overexposed regions are left, and the iteration stops. Thus, we can reconstruct complete 3-D data without being bothered by saturation.

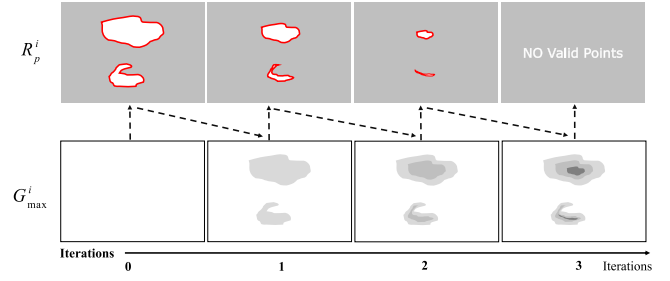


Fig. 4. Schematic of the iterative adjustment for the maximum input grayscale and the overexposed region.

D. Optimized Projection Intensity Based on Surface Reflectance

Since we reduce the projected brightness discretely, this can lead to phase errors arising from abrupt changes in projection intensity. To solve this problem, we propose a method that uses the reflectance map $r(u^c, v^c)$ with continuous variation and maps it from the camera coordinate system to the projector coordinate system based on the reconstructed 3-D data so that the projection intensity changes gently. Thus, accurate reflectance analysis is critical to reducing overexposure imaging.

To exclude the effects of reflected and ambient light from solving for reflectance, we rewrite (3) as follows:

$$I_n^c = x_1 I_n^p + x_2. \quad (18)$$

Here, $x_1 = r$ and $x_2 = ra + b$. In this way, $r(u^c, v^c)$ can be determined by projecting a series of patterns with known grayscale I_n^p and the captured I_n^c based on the minimization of the following cost function F_r :

$$F_r = \arg \min_{x_1, x_2} \sum_{i=1}^n \|I_i^c - (x_1 I_i^p + x_2)\|^2. \quad (19)$$

Consequently, the solution to (x_1, x_2) can be calculated by solving the following equation:

$$\begin{bmatrix} I_1^p & 1 \\ \vdots & \vdots \\ I_n^p & 1 \end{bmatrix} \begin{bmatrix} x_1 \\ x_2 \end{bmatrix} = \begin{bmatrix} I_1^c \\ \vdots \\ I_n^c \end{bmatrix}, \quad n \geq 2. \quad (20)$$

This is a fast process, enabling us to gather $r(u^c, v^c)$ effectively. Then, the map is mapped to the projector space, resulting in $r(u^p, v^p)$, which can be used to adjust the projection intensity on a pixel-by-pixel basis. Consequently, the new brightness distribution G^N can be calculated as

$$G^N(u^p, v^p) = 255 - N \times g \times \bar{r}(u^p, v^p). \quad (21)$$

Here, N is the total number of iterations, and $\bar{r}(u^p, v^p)$ is the normalized surface intensity. Then, the phase-shifted fringe patterns can be obtained based on G^N through

$$I_n^p(u^p, v^p) = G^N(u^p, v^p) \times [a^p + b^p \cos(2\pi f^p u^p - \delta^n)]. \quad (22)$$

The improved quality of the fringe patterns generated through this process enables the acquisition of more complete and continuous 3-D data from high-dynamic reflective surfaces.

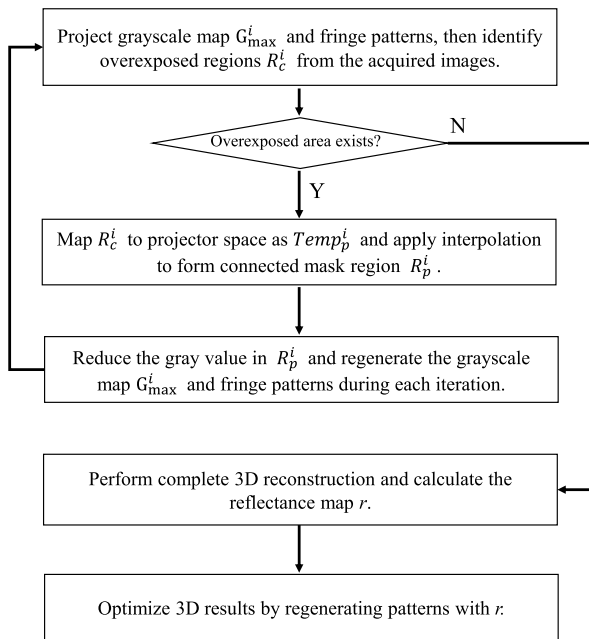


Fig. 5. Flowchart of the iterative optimization and 3-D reconstruction based on the reflectance information.

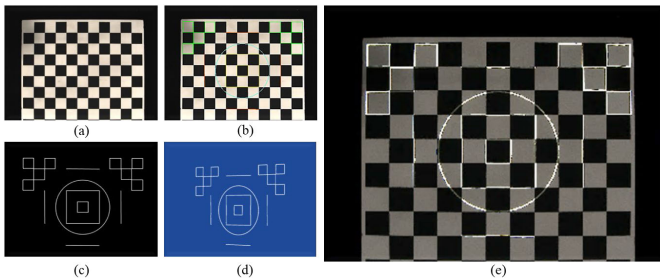


Fig. 6. Diagram of inverse labeling using a white light projector. (a) Image of the calibration board. (b) Calibration board with labeling lines at the boundary of the square pattern. (c) Interactive lines with the background removed. (d) Marker pattern mapped to the DMD plane. (e) Projecting the image of (d) onto the sample.

Fig. 5 illustrates a flowchart of the iterative optimization and 3-D reconstruction based on the reflectance information. This process aims to detect and correct overexposed regions, improving the accuracy of the encoded fringe patterns and thus optimizing the final 3-D reconstruction results.

E. Interactive Guidance Based on Marker Inverse Labeling

Based on the calibrated optical path depicted in Fig. 3(e), we can directly transform interactive markers on the image to the DMD plane. Subsequently, these markers are projected onto the sample surface via the projector, as shown in Fig. 6. This process enables a new mode of immersive and location-accurate remote interaction guidance for precisely cutting pathological samples.

The width and shape of the marking line can be adjusted in real time through the software interface. The brightness distribution of the mark can be adaptively adjusted based on the brightness distribution of the sample. However, due to the current projection device's reliance on white light, only white

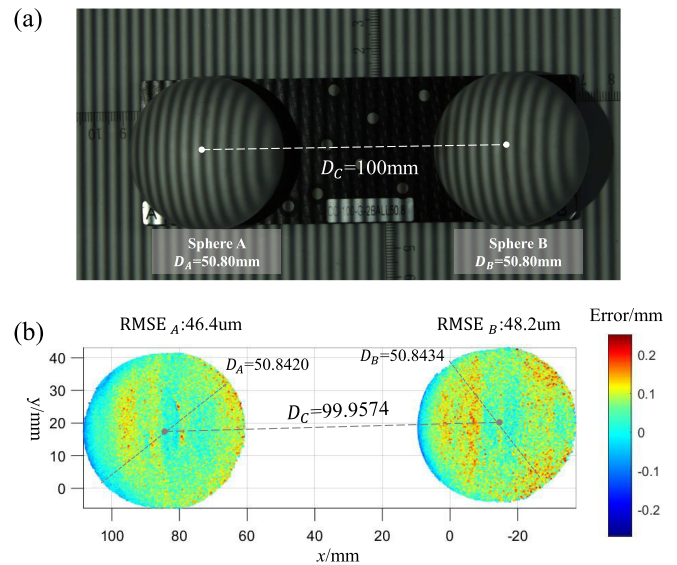


Fig. 7. Accuracy measurement of standard spheres. (a) Photograph of the standard spheres. (b) Measured 3-D result and error analysis.

marks can be projected; color marks are not yet supported. In this article, we demonstrate the inverse labeling function using a calibration board to illustrate its accuracy. Further experimental results will be presented in Section V.

IV. RESULTS

This section first presents experiments on calibration, methods comparison, and 3-D reconstruction for some highly reflective objects using the proposed adaptive projection algorithm, including a flat plate and multiple tissues. Then, we demonstrate the application of inverse labeling in interactive guidance using biological samples, highlighting the versatility and accuracy of the labeling function. We emphasize here that the tissue samples used in the experiment were all obtained from local fresh markets.

A. Accuracy Evaluations by Measuring Standard Spheres

To assess the system's accuracy, we used two custom standard spheres labeled A and B, each with a nominal diameter of 50.80 mm and a precise center-to-center distance of 100 mm, as shown in Fig. 7(a). Fig. 7(b) provides an error map of the sphere fitting process, visually depicting the error distribution across the sphere surfaces between the fit and actual measured results. Through the color distribution, it can be observed that the majority of the surface errors fall within $\pm 0.2\text{mm}$, indicating a high-quality fit of the spheres. The measured diameters are 50.8420 mm for sphere A and 50.8434 mm for sphere B, with a center-to-center distance of 99.9574 mm, resulting in a relative error of 0.0426%. Additionally, the root-mean-square error (RMSE) between the fit and measured diameters was determined to be $46.4\mu\text{m}$ for sphere A and $48.2\mu\text{m}$ for sphere B. Such measurement accuracy is sufficient to support the requirements of our systems in their applicable applications.

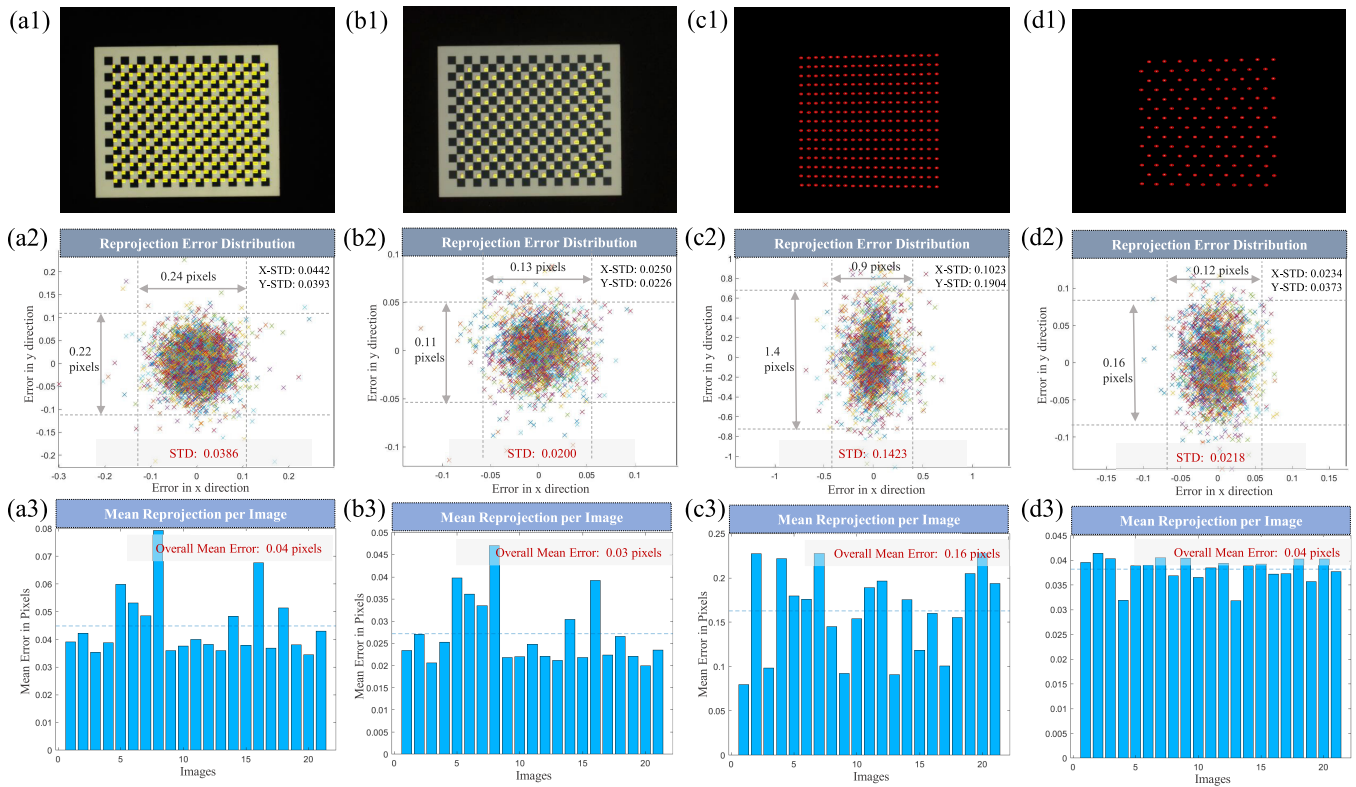


Fig. 8. Calibration results using chessboard corners and geometric center points. Each row presents feature point positions, reprojection error distributions, and errors across multiple calibration poses. (a1)–(a3) Camera calibration with chessboard corners. (b1)–(b3) Camera calibration with the geometric center points. (c1)–(c3) Projector calibration with chessboard corners. (d1)–(d3) Projector calibration with geometric center points.

B. System Calibration of the Proposed Method

This section presents a comparison between the calibration results obtained using chessboard corners and geometric center points while utilizing local homography transformation as the calibration feature. Fig. 8(a1)–(a3) and (b1)–(b3) illustrates the performance of different feature points in camera calibration, while Fig. 8(c1)–(c3) and (d1)–(d3) demonstrates their effects on projector calibration. Compared to chessboard corners, intersection points based on local homography transformation exhibit a stronger aggregation in feature point distribution, with the camera’s standard deviation (STD) decreasing from 0.0386 to 0.02 pixels. The reprojection error of the projector decreases from 0.16 to 0.04 pixels, and the STD values for all points also show a significant reduction, indicating superior accuracy, thus validating the effectiveness of the selected feature points in enhancing system calibration precision.

C. Experiment on a Plate With Different Surface Reflectances

We utilized a planar plate to validate our methods. Fig. 9(a) depicts a custom-designed plate with different surface reflectances by featuring squares of different grayscales on the left and rectangles exhibiting distinct colors on the right. The experimental objects and the results at different stages are presented in Fig. 9(b)–(g). After converting camera pixels to projector coordinates, as shown in Fig. 9(e), the overexposed regions in the DMD plane can be obtained, as shown in Fig. 9(f). With the corresponding exposure area identified on

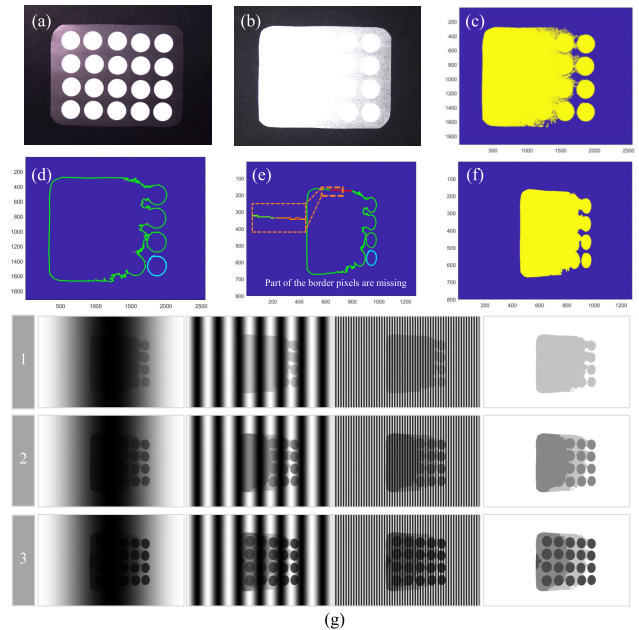


Fig. 9. Overexposed area mapping of a planar plate containing different intensities and colors using the adaptive projection algorithm. (a) Image of the measured sample. (b) Sample image under uniform white light illumination. (c) Overexposed regions marked by yellow color. (d) Extracted boundary of the overexposure region. (e) Mask boundaries mapped to projectors. (f) Overexposed regions in DMD plane. (g) Phase-shifting patterns generated during three iterations.

the DMD, we generated new patterns through three iterative processes, as shown in Fig. 9(g).

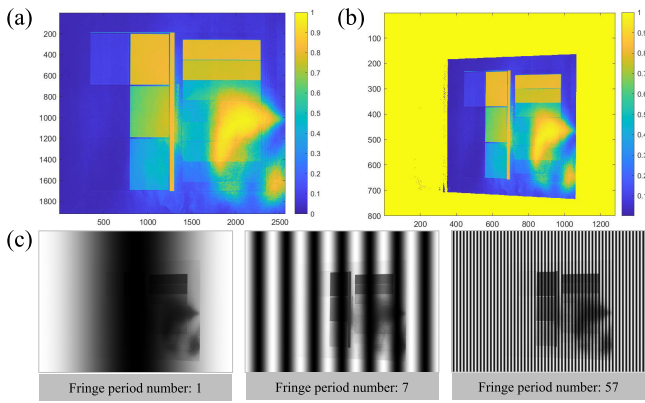


Fig. 10. Projection patterns are optimized by using the reflectance map of the sample surface. (a) Reflectance map on the camera plane. (b) Reflectance map on the DMD plane. (c) Fringe patterns optimized based on the reflectance map.

Based on the 3-D data built after three iterations, the reflectance map on the camera plane, as shown in Fig. 10(a), was mapped to the DMD plane, as shown in Fig. 10(b). Fringe patterns with different frequencies and intensity distributions were adaptively generated from the reflectance data, as shown in Fig. 10(c). Note that the fringe map in Fig. 10(c) was re-optimized based on the reflectance map, which can avoid phase errors arising from abrupt changes in projection intensity. This is different from the result obtained by directly reducing the intensity distribution in Fig. 9(g).

The newly generated phase-shifting patterns were then projected onto the sample to be compared with conventional methods. Our approach significantly enhances the visual quality and contrast of the image, as demonstrated in Fig. 11(a) and (b). Subsequent 3-D reconstructions were then obtained using our method and compared with the results obtained without applying special algorithms, as shown in Fig. 11(c) and (d). The result indicates that the integrity of 3-D reconstruction has been dramatically improved.

D. 3-D Reconstruction of a Fish Maw and Pig Kidney With Highly Reflective Surfaces

In this section, we selected a fish maw and a pig kidney as the samples for testing. These samples are motivated by their biological tissue-like characteristics, including a smooth surface and similar reflectance properties to human tissue, making them ideal samples for simulating biological 3-D imaging. Our method was tested on a maw sample first, and the results are shown in Fig. 12. The reduction in overexposure in 3-D reconstruction is shown in Fig. 12(a). The red line on the sample surface was selected to illustrate the effect of modulating the sinusoidal fringe waveform to avoid saturation. As shown in Fig. 12(b), the intensity along the red line decreases over three iterations, forming phase-shifting intensities with appropriate amplitude to avoid phase errors. As shown in Fig. 12(c), the height values for the missing areas were initially set to zero. Observing how the height distribution changes along the red line during the iterative process, we can see that it gradually becomes continuous. This

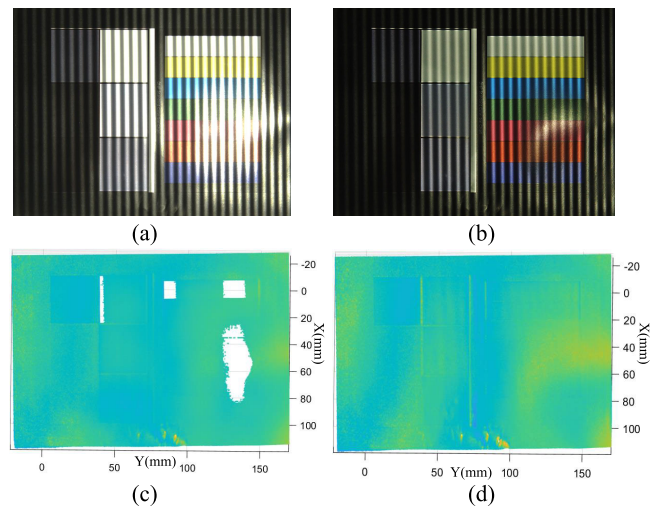


Fig. 11. Comparison of the 3-D results for the custom-designed plate using the traditional FFP method and our improved adaptive projection method. (a) Sample image exhibiting saturation under standard fringe illumination. (b) Sample image without saturation under regenerated fringe illumination. (c) Reconstructed 3-D result with obvious errors using the patterns in (a). (d) Reconstructed 3-D result using the optimized fringe patterns.

experimental result demonstrates that our method effectively employs adaptive projection intensities for different reflectance regions, significantly enhancing the adaptability of 3-D imaging for highly reflective targets.

Let us focus on reflectance; by projecting five gray patterns with intensities of 255, 195, 135, 75, and 15, respectively, the reflectance distribution map of the sample surface was obtained, as shown in Fig. 13(a). The fringe patterns regenerated based on this reflectance map, as shown in Fig. 13(b), were projected onto the sample surface. The captured image is illustrated in Fig. 13(c). The complete 3-D reconstruction result obtained through the iterative processing is shown in Fig. 13(d). Notably, the 3-D result derived from fringe patterns based on reflectance intensity, as shown in Fig. 13(e), is smoother and more accurate. This optimization can eliminate potential phase errors from abrupt variations in projection intensities.

We also conducted experiments on a pig kidney, as shown in Fig. 14. We concisely compared images with saturation and images with the optimized projection pattern. When the background brightness is consistent, if no special means are taken, the highly reflective nature of the sample causes the brightness of the fringe to exceed the camera's threshold, as shown in Fig. 14(a). In contrast, the image taken under adaptive fringe projection shows better contrast consistency, as shown in Fig. 14(b). The validity of our method is clearly and equally confirmed through the corresponding 3-D results, demonstrating excellent 3-D imaging capability for various biological tissues.

E. Comparison of the Proposed Method With Others

We compared our method with several other typical methods to examine its performance (including Lin et al.'s [26] adaptive digital fringe projection (ADFP) method and Du et al.'s [41]

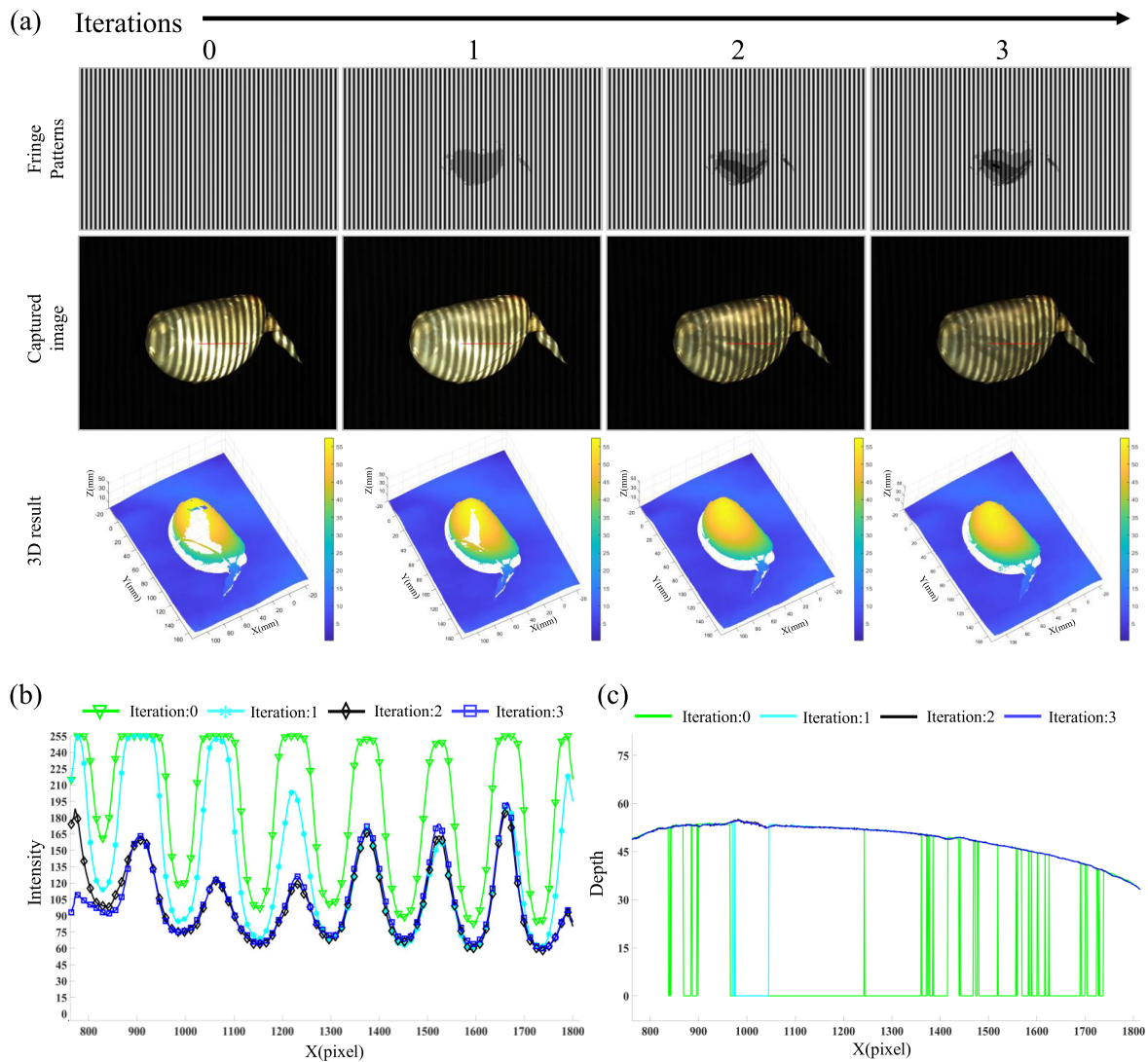


Fig. 12. Proposed adaptive projection was employed in reconstructing a fish maw, with intensity and depth sections changing along the red line. (a) Projected fringe pattern, captured sample image, and the 3-D data obtained during the adaptive projection process. (b) Intensity variation along the red line during the adaptive projection process. (c) Depth variation along the red line during the adaptive projection process.

multiple exposure fusion method). Fig. 15 presents the comparison results. From Fig. 15(a) and (b), it can be observed that the traditional multiple exposure method generates fringe patterns with uneven brightness. In contrast, Fig. 15(c) and (d) shows the results of Lin et al.'s [26] ADFP and proposed methods, respectively. The proposed method demonstrates superior fringe contrast, particularly in complex geometric regions. Fig. 15(e)–(h) further illustrates the 3-D reconstruction results using different methods. The proposed method excels in detailed reproduction compared to other methods, especially regarding accuracy along edges and curved surfaces.

Fig. 16 further shows the comparison of the reconstruction completeness achieved by these methods. Fig. 16(a) displays the spatial distribution of reconstruction results within the region of interest (ROI). Although the overall trends of different methods are consistent, notable differences can still be observed in the local ROI (see the zoomed-in view region). The proposed method demonstrates smoother fitting in local details and exhibits the highest stability and consistency in

edge areas, indicating its advantage in handling complex geometric structures.

We define the reconstruction ratio as the number of reconstructed point cloud points (numerator) divided by the total number of pixels representing the metallic object in 2-D (denominator). The bar chart in Fig. 16(b) clearly illustrates the reconstruction rates of the four methods, offering a quantitative assessment. The proposed method achieves the highest reconstruction rate of 97.93%, outperforming the other methods. The full brightness method yields the lowest reconstruction rate at 85.40%, while the multiple exposures and Lin et al.'s [26] ADFP methods achieve 97.12% and 91.37%, respectively.

F. Interactive Inverse Labeling Through Marker Projection

To provide a better remote guidance experience, we need to perform accurate on-site light labeling projections based on our reconstructed 3-D results. Experiments were conducted on several biological samples, including pig kidney, pork liver,

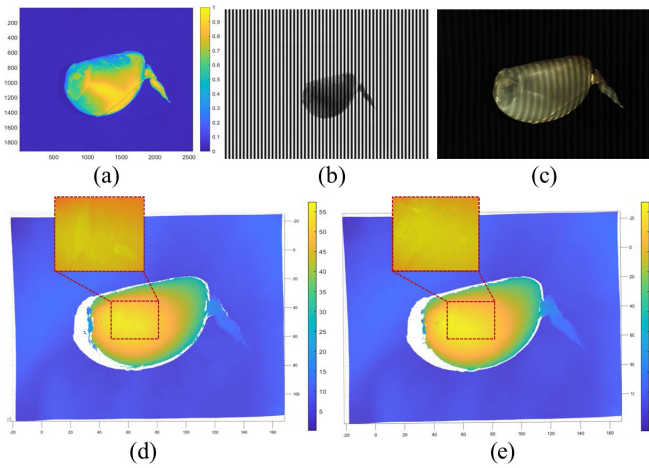


Fig. 13. Intensity adjustment of the projection pattern based on the reflectance map. (a) Reflectance map of the sample surface. (b) Adaptive fringe patterns generated from the reflectance map. (c) Captured image by using the fringe patterns in (b). (d) Reconstructed 3-D data were obtained after iterative processing. (e) Reconstructed 3-D data were obtained using adaptive fringe patterns.

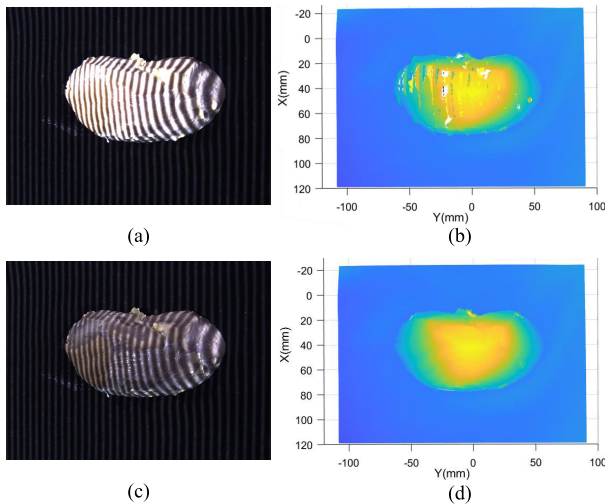


Fig. 14. Comparison of fringe images and 3-D results of a pig kidney. (a) and (b) One of the overexposed fringe images and 3-D data obtained using them, respectively. (c) and (d) One of the adaptive fringe images and 3-D data obtained using them.

and chicken hearts, to evaluate the precision and versatility of our system for interactive inverse labeling.

The results are presented in Fig. 17(a1)–(c1); following this, interactive multiple lines were drawn on the images, as shown in Fig. 17(a2)–(c2), and projected onto the sample to illustrate the function of inverse labeling, as shown in Fig. 17(a3)–(c3), in which “Area 1”–“Area 4” are enlarged as shown in Fig. 17(d1)–(d4). Our software can customize the linewidth and style to suit specific application environments. Besides, some commonly used symbols, such as arrows, rectangles, and circles, can be called directly by the user, providing significant convenience. The experimental results confirm our system’s effectiveness in providing telemedicine services. Its high accuracy and ability to achieve 3-D imaging based on adaptive fringe projection for biological tissues demonstrate its ability for reliable remote healthcare delivery.

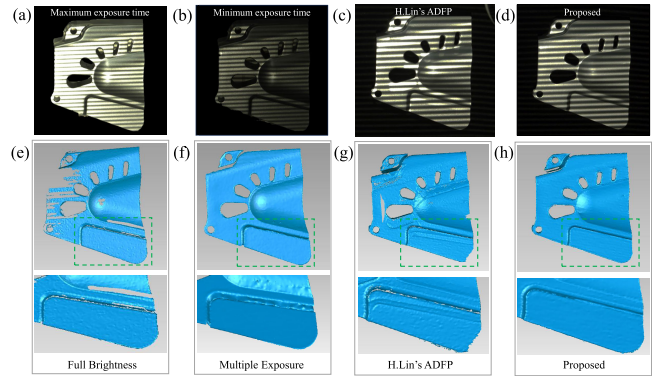


Fig. 15. Comparison of the proposed method with the results of other methods. (a) and (b) Image captured at minimum and maximum exposure times using the multiple exposure method. (c) Image obtained with Lin et al.’s [26] ADFP method. (d) Image captured by our proposed method. (e)–(h) 3-D reconstruction results from the traditional, multiple exposures, ADFP, and our methods, respectively.

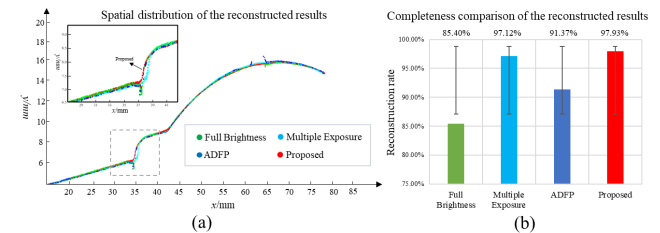


Fig. 16. Details and reconstruction ratio comparison using different methods. (a) Spatial distribution of the reconstruction at the ROI. (b) Comparison of the reconstruction ratio.

V. DISCUSSION

A. Selection of the Reduction Value in the Iterative Process

In the adaptive fringe projection algorithm, the reduced value of projection intensity significantly influences the efficiency of the iteration and the final 3-D result. Although a minor intensity reduction improves the accuracy, the calculation time is extended due to the increased iterations, which may lead to decreased efficiency when dealing with higher dynamic samples. Conversely, a more significant reduction speeds up the iterations, but the details and accuracy of the mapping may be sacrificed. Therefore, a tradeoff must be made when choosing an intensity reduction to ensure that the 3-D results are as accurate as possible while maintaining a reasonable computational speed. This article chooses a constant reduction value of 60 based on comprehensive consideration of this tradeoff to achieve efficient and accurate 3-D reconstruction.

B. Adaptive Fringe Generation by Intensity Reduction or Reflectance Guidance

During multiple iterations, adaptive fringe generation through constant intensity reduction can cause intensity jumps in the boundary where brightness changes. This can lead to a loss or distortion of detail, particularly in complex or height-varying areas. In contrast, the reflectance-guided process leverages the continuous reflectance change to achieve pixelwise adjustment of the projection intensity. This approach

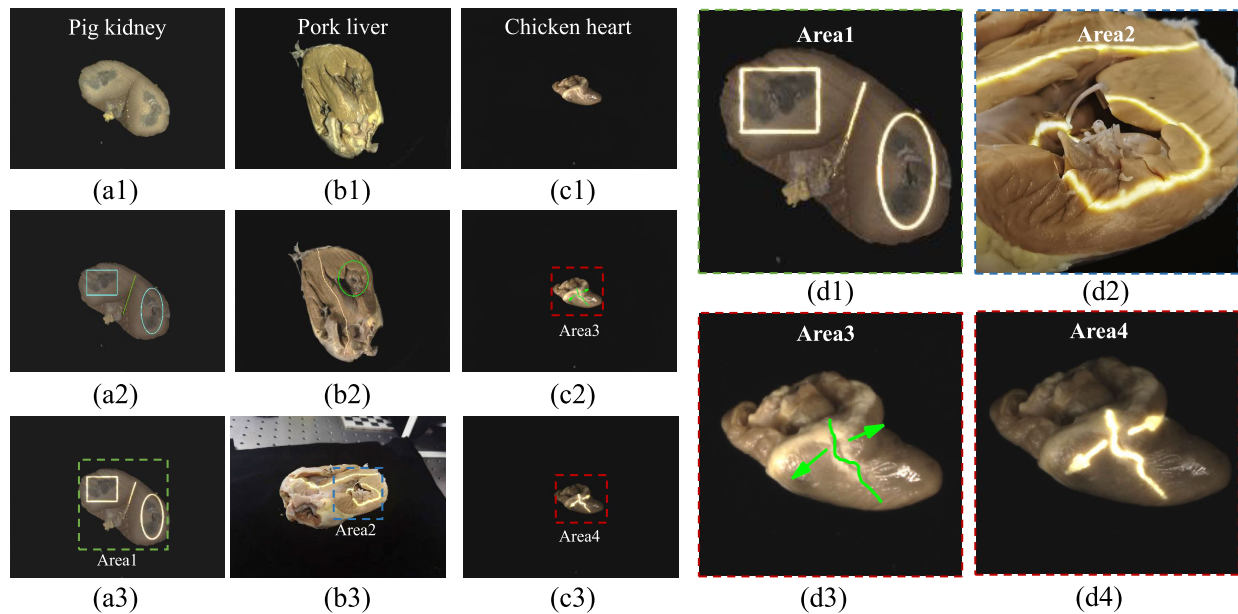


Fig. 17. Interactive inverse labeling test on different tissues. (a1)–(c1) Sample image of the pig kidney, pork liver, and chicken heart. (a2)–(c2) Interactive guidance lines drawn on the images. (a3)–(c3) Marker light is projected onto the sample. (d1)–(d4) Enlarged image of “Area 1”–“Area 4” on the samples.

allows for more accurate surface characteristic representation, enhancing the overall quality of the reconstructed 3-D data and producing a more realistic final result. However, it takes a little extra time to calculate the reflectance map.

C. Parameters Choice of the Optical Devices

In our system, the camera resolution is 2560 1920, and the maximum horizontal resolution of the projector is 1280. When designing the system, it is crucial to consider the projector and camera’s digital resolution fully. Two key factors to consider are cost and resolution. High-resolution projectors and cameras offer significant advantages in terms of high-quality optics and images but also have a high economic cost. Therefore, it is essential to match the camera and projector resolution. If the camera resolution is significantly higher than the projector, multiple pixels map to the same projector pixel, leading to information redundancy. Conversely, a lower camera resolution results in losing the projector’s optical information. Therefore, setting the camera and projector resolution reasonably is a critical factor in improving the overall system performance and an effective means to reduce costs.

VI. CONCLUSION

This article tackles the issue of image saturation during the 3-D reconstruction of highly dynamic surfaces by introducing a novel adaptive projection approach. This approach requires only pixel intensity adjustments on the projection pattern without additional optical equipment. An interactive guidance method utilizing 3-D data is proposed. It allows users to draw various markers on a 2-D image and project them onto the sample, facilitating remote operation guidance like sample sectioning.

While the current setup has a relatively fixed field of view, future research will focus on developing 3-D imaging

methods with a variable field of view. Developing an adaptive brightness reduction algorithm for overexposed regions would further enhance the usable range of fringe modulation and improve the usage of the image quantization range.

REFERENCES

- [1] R. J. Hocken and P. H. Pereira, *Coordinate Measuring Machines and Systems*, vol. 2. Boca Raton, FL, USA: CRC Press, 2012.
- [2] Z. Chen and M. Segev, “Highlighting photonics: Looking into the next decade,” *eLight*, vol. 1, no. 1, p. 2, Jun. 2021, doi: [10.1186/s43593-021-00002-y](https://doi.org/10.1186/s43593-021-00002-y).
- [3] Y. Li, J. Qian, S. Feng, Q. Chen, and C. Zuo, “Deep-learning-enabled dual-frequency composite fringe projection profilometry for single-shot absolute 3D shape measurement,” *Opto-Electron. Adv.*, vol. 5, no. 5, p. 210021, 2022.
- [4] S. Zhang, “High-speed 3D shape measurement with structured light methods: A review,” *Opt. Lasers Eng.*, vol. 106, pp. 119–131, Jul. 2018.
- [5] S. Van der Jeught and J. J. J. Dirckx, “Real-time structured light profilometry: A review,” *Opt. Lasers Eng.*, vol. 87, pp. 18–31, Dec. 2016, doi: [10.1016/j.optlaseng.2016.01.011](https://doi.org/10.1016/j.optlaseng.2016.01.011).
- [6] W. Flores-Fuentes et al., “3D spatial measurement for model reconstruction: A review,” *Measurement*, vol. 207, Feb. 2023, Art. no. 112321, doi: [10.1016/j.measurement.2022.112321](https://doi.org/10.1016/j.measurement.2022.112321).
- [7] R. Yang, S. Cheng, W. Yang, and Y. Chen, “Robust and accurate surface measurement using structured light,” *IEEE Trans. Instrum. Meas.*, vol. 57, no. 6, pp. 1275–1280, Jun. 2008, doi: [10.1109/TIM.2007.915103](https://doi.org/10.1109/TIM.2007.915103).
- [8] F. Gutierrez-Barragan, H. Chen, M. Gupta, A. Velten, and J. Gu, “IToF2dToF: A robust and flexible representation for data-driven time-of-flight imaging,” *IEEE Trans. Comput. Imag.*, vol. 7, pp. 1205–1214, 2021, doi: [10.1109/TCI.2021.3126533](https://doi.org/10.1109/TCI.2021.3126533).
- [9] Y. Hu et al., “Structured light 3D imaging instrument for biological tissues with potential application in telemedicine,” *IEEE Trans. Instrum. Meas.*, vol. 73, pp. 1–11, 2024, doi: [10.1109/TIM.2023.3331396](https://doi.org/10.1109/TIM.2023.3331396).
- [10] P. Liu, K. Zhang, B. Zhao, M. Li, and Y. Chen, “Self-coding phase shift for absolute phase retrieval in fringe projection profilometry,” *IEEE Trans. Instrum. Meas.*, vol. 72, pp. 1–10, 2023, doi: [10.1109/TIM.2023.3317476](https://doi.org/10.1109/TIM.2023.3317476).
- [11] G. M. Brown, “Overview of three-dimensional shape measurement using optical methods,” *Opt. Eng.*, vol. 39, no. 1, p. 10, Jan. 2000.
- [12] A.-H. Nguyen, K. L. Ly, C. Qiong Li, and Z. Wang, “Single-shot 3D shape acquisition using a learning-based structured-light technique,” *Appl. Opt.*, vol. 61, no. 29, p. 8589, Oct. 2022, doi: [10.1364/ao.470208](https://doi.org/10.1364/ao.470208).

- [13] J. Yu and F. Da, "Absolute phase unwrapping for objects with large depth range," *IEEE Trans. Instrum. Meas.*, vol. 72, pp. 1–10, 2023, doi: [10.1109/TIM.2023.3271764](https://doi.org/10.1109/TIM.2023.3271764).
- [14] P. S. Huang, "Novel method for structured light system calibration," *Opt. Eng.*, vol. 45, no. 8, Aug. 2006, Art. no. 083601, doi: [10.1117/1.2336196](https://doi.org/10.1117/1.2336196).
- [15] Y. Hu, Q. Chen, S. Feng, T. Tao, A. Asundi, and C. Zuo, "A new microscopic telecentric stereo vision system—calibration, rectification, and three-dimensional reconstruction," *Opt. Lasers Eng.*, vol. 113, pp. 14–22, Feb. 2019.
- [16] B. Li and S. Zhang, "Structured light system calibration method with optimal fringe angle," *Appl. Opt.*, vol. 53, no. 33, p. 7942, Nov. 2014, doi: [10.1364/ao.53.007942](https://doi.org/10.1364/ao.53.007942).
- [17] H. Huang, B. Niu, S. Cheng, and F. Zhang, "Adaptive pixel-by-pixel modulated 3-D morphometry based on digital micromirror device," *IEEE Trans. Instrum. Meas.*, vol. 73, pp. 1–10, 2024, doi: [10.1109/TIM.2024.3368489](https://doi.org/10.1109/TIM.2024.3368489).
- [18] S. Feng, L. Zhang, C. Zuo, T. Tao, Q. Chen, and G. Gu, "High dynamic range 3D measurements with fringe projection profilometry: A review," *Meas. Sci. Technol.*, vol. 29, no. 12, Dec. 2018, Art. no. 122001, doi: [10.1088/1361-6501/aae4fb](https://doi.org/10.1088/1361-6501/aae4fb).
- [19] Y. Fu, J. Fan, F. Jing, and M. Tan, "High dynamic range structured light 3-D measurement based on region adaptive fringe brightness," *IEEE Trans. Ind. Electron.*, vol. 71, no. 7, pp. 8080–8090, Jul. 2024, doi: [10.1109/TIE.2023.3303655](https://doi.org/10.1109/TIE.2023.3303655).
- [20] P. Xu, J. Liu, and J. Wang, "High dynamic range 3D measurement technique based on adaptive fringe projection and curve fitting," *Appl. Opt.*, vol. 62, no. 13, p. 3265, May 2023, doi: [10.1364/AO.488583](https://doi.org/10.1364/AO.488583).
- [21] Z. Wu, W. Guo, and Q. Zhang, "Two-frequency phase-shifting method vs. Gray-coded-based method in dynamic fringe projection profilometry: A comparative review," *Opt. Lasers Eng.*, vol. 153, Jun. 2022, Art. no. 106995, doi: [10.1016/j.optlaseng.2022.106995](https://doi.org/10.1016/j.optlaseng.2022.106995).
- [22] S.-T. Yau, "High dynamic range scanning technique," *Opt. Eng.*, vol. 48, no. 3, Mar. 2009, Art. no. 033604.
- [23] L. Rao and F. Da, "High dynamic range 3D shape determination based on automatic exposure selection," *J. Vis. Commun. Image Represent.*, vol. 50, pp. 217–226, Jan. 2018, doi: [10.1016/j.jvcir.2017.12.003](https://doi.org/10.1016/j.jvcir.2017.12.003).
- [24] J. Wang, Y. Zhou, and Y. Yang, "A novel and fast three-dimensional measurement technology for the objects surface with non-uniform reflection," *Results Phys.*, vol. 16, Mar. 2020, Art. no. 102878.
- [25] C. Waddington and J. Kofman, "Saturation avoidance by adaptive fringe projection in phase-shifting 3D surface-shape measurement," in *Proc. Int. Symp. Optomechatronic Technol.*, Oct. 2010, pp. 1–4, doi: [10.1109/ISOT.2010.5687390](https://doi.org/10.1109/ISOT.2010.5687390).
- [26] H. Lin, J. Gao, Q. Mei, Y. He, J. Liu, and X. Wang, "Adaptive digital fringe projection technique for high dynamic range three-dimensional shape measurement," *Opt. Exp.*, vol. 24, no. 7, p. 7703, Apr. 2016, doi: [10.1364/oe.24.007703](https://doi.org/10.1364/oe.24.007703).
- [27] H. Lin, J. Gao, Q. Mei, G. Zhang, Y. He, and X. Chen, "Three-dimensional shape measurement technique for shiny surfaces by adaptive pixel-wise projection intensity adjustment," *Opt. Lasers Eng.*, vol. 91, pp. 206–215, Apr. 2017, doi: [10.1016/j.optlaseng.2016.11.015](https://doi.org/10.1016/j.optlaseng.2016.11.015).
- [28] T. Cheng, L. Qin, Y. Li, J. Hou, and C. Xiao, "An adaptive multiexposure scheme for the structured light profilometry of highly reflective surfaces using complementary binary gray code," *IEEE Trans. Instrum. Meas.*, vol. 73, pp. 1–12, 2024, doi: [10.1109/TIM.2024.3351252](https://doi.org/10.1109/TIM.2024.3351252).
- [29] Y. Liu, Y. Fu, X. Cai, K. Zhong, and B. Guan, "A novel high dynamic range 3D measurement method based on adaptive fringe projection technique," *Opt. Lasers Eng.*, vol. 128, May 2020, Art. no. 106004.
- [30] S. Zhang, Y. Yang, W. Shi, L. Feng, and L. Jiao, "3D shape measurement method for high-reflection surface based on fringe projection," *Appl. Opt.*, vol. 60, no. 34, p. 10555, 2021.
- [31] J. Sun and Q. Zhang, "A 3D shape measurement method for high-reflective surface based on accurate adaptive fringe projection," *Opt. Lasers Eng.*, vol. 153, Jun. 2022, Art. no. 106994, doi: [10.1016/j.optlaseng.2022.106994](https://doi.org/10.1016/j.optlaseng.2022.106994).
- [32] B. Salahieh, Z. Chen, J. J. Rodriguez, and R. Liang, "Multi-polarization fringe projection imaging for high dynamic range objects," *Opt. Exp.*, vol. 22, no. 8, pp. 10064–10071, 2014, doi: [10.1364/OE.22.010064](https://doi.org/10.1364/OE.22.010064).
- [33] S.-B. Zhao, L.-Y. Liu, and M.-Y. Ma, "Adaptive high-dynamic range three-dimensional shape measurement using DMD camera," *IEEE Access*, vol. 7, pp. 67934–67943, 2019, doi: [10.1109/ACCESS.2019.2918843](https://doi.org/10.1109/ACCESS.2019.2918843).
- [34] Y. Hu, Q. Chen, Y. Liang, S. Feng, T. Tao, and C. Zuo, "Microscopic 3D measurement of shiny surfaces based on a multi-frequency phase-shifting scheme," *Opt. Lasers Eng.*, vol. 122, pp. 1–7, Nov. 2019, doi: [10.1016/j.optlaseng.2019.05.019](https://doi.org/10.1016/j.optlaseng.2019.05.019).
- [35] Y. Zheng, Y. Wang, V. Suresh, and B. Li, "Real-time high-dynamic-range fringe acquisition for 3D shape measurement with a RGB camera," *Meas. Sci. Technol.*, vol. 30, no. 7, May 2019, Art. no. 075202, doi: [10.1088/1361-6501/ab0ced](https://doi.org/10.1088/1361-6501/ab0ced).
- [36] C. Jiang, T. Bell, and S. Zhang, "High dynamic range real-time 3D shape measurement," *Opt. Exp.*, vol. 24, no. 7, pp. 7337–7346, Mar. 2016, doi: [10.1364/OE.24.007337](https://doi.org/10.1364/OE.24.007337).
- [37] C. Zuo, L. Huang, M. L. Zhang, Q. Chen, and A. Asundi, "Temporal phase unwrapping algorithms for fringe projection profilometry: A comparative review," *Opt. Lasers Eng.*, vol. 85, pp. 84–103, Oct. 2016, doi: [10.1016/j.optlaseng.2016.04.022](https://doi.org/10.1016/j.optlaseng.2016.04.022).
- [38] Z. Zhang, "A flexible new technique for camera calibration," *IEEE Trans. Pattern Anal. Mach. Intell.*, vol. 22, no. 11, pp. 1330–1334, 2002.
- [39] H. Deng, P. Hu, G. Zhang, C. Xia, Y. Cai, and S. Yang, "Accurate and flexible calibration method for a 3D microscopic structured light system with telecentric imaging and scheimpflug projection," *Opt. Exp.*, vol. 31, no. 2, p. 3092, Jan. 2023, doi: [10.1364/oe.480333](https://doi.org/10.1364/oe.480333).
- [40] F. Youyang, W. Qing, Y. Yuan, and Y. Chao, "Robust improvement solution to perspective-n-point problem," *Int. J. Adv. Robotic Syst.*, vol. 16, no. 6, Nov. 2019, Art. no. 1729881419885700, doi: [10.1177/1729881419885700](https://doi.org/10.1177/1729881419885700).
- [41] J. Du, F. Yang, H. Guo, J. Zhu, and P. Zhou, "Parameter selection on a multi-exposure fusion method for measuring surfaces with varying reflectivity in microscope fringe projection profilometry," *Appl. Opt.*, vol. 63, no. 13, p. 3506, May 2024.



Ziqiang Wei received the bachelor's degree in optoelectronic information science and engineering from Anhui Normal University, Wuhu, China, in 2022.

His research interests focus on 3-D measurement with structured light and computer vision.



Sudong Ding received the bachelor's degree in optoelectronic information science and engineering from Anhui Normal University, Wuhu, China, in 2023. He is currently pursuing the master's degree in optoelectronic information engineering with Nanjing University of Science and Technology, Nanjing, China.



Yan Hu received the Ph.D. degree in optical engineering from Nanjing University of Science and Technology, Nanjing, China, in 2019.

He has been supported by the Young Elite Scientists Sponsorship Program by China Association for Science and Technology (CAST). His research interests include 3-D sensing, computational optoelectronic imaging, and image processing.

Dr. Hu received the Young Optical Science and Technology Award from Jiangsu Optics Society.



Shuang Mu received the master's degree in optoelectronic information engineering from Nanjing University of Science and Technology, Nanjing, China, in 2023.

He currently works with Shanghai Aerospace Control Technology Institute, Shanghai, China. He is mainly engaged in the research and work of space photoelectric sensor.



Shijie Feng (Member, IEEE) received the Ph.D. degree in optical engineering from Nanjing University of Science and Technology, Nanjing, China, in 2017.

He is currently a Professor at Nanjing University of Science and Technology. His research focuses on high-speed 3D measurement techniques based on fringe projection.

Dr. Feng was nominated for the fourth "National Excellent Doctoral Dissertation" in Optical Engineering in 2019 and received the Young Optical Science and Technology Award from Jiangsu Optical Society in 2020.



Kehui Wang received the bachelor's degree in computer and science from Ludong University, Yantai, China, in 2005, and the master's degree in computer applied technology from Harbin Engineering University, Harbin, China, in 2008.

His research interests include software engineering, medical image analysis, and embedded systems of medical instruments.



Qian Chen is currently a Chang Jiang Scholar and a Professor with Nanjing University of Science and Technology, Nanjing, China. His research interests include night vision technology, photoelectric devices, and image processing.

Dr. Chen was awarded the Second Prize of the National Science and Technology Progress in 2008, the Second Prize of the National Technical Invention in 2018, and the National Innovation Award in 2020.



Kun Gui received the bachelor's degree in computer and science and the master's degree in computer applied technology from Harbin Engineering University, Harbin, China, in 2007 and 2010, respectively.

His research interests include medical image analysis, big data analysis, and deep learning techniques.



Chao Zuo (Senior Member, IEEE) is currently a Chang Jiang Scholar and a Professor with Nanjing University of Science and Technology, Nanjing, China, and also the Group Leader of the Smart Computational Imaging Laboratory. His research interests include computational imaging and optical information processing technology.

Dr. Zuo has been selected by the Natural Science Foundation of China (NSFC) for Excellent Young Scholars and Outstanding Youth Foundation of Jiangsu Province.